

FULL PAPER

Open Access



# Relation between earthquake swarm activity and tides in the Noto region, Japan

Fuyuki Hirose<sup>1\*</sup> , Koji Tamaribuchi<sup>1</sup> , Akio Kobayashi<sup>2</sup> and Kenji Maeda<sup>1</sup>

## Abstract

The Noto region in Japan has been experiencing earthquake swarm activity since mid-2018, with repeated rises and falls in activity. Crustal deformation (expansion and uplift) observed there since the end of 2020 has been connected to crustal fluids. Studies in other regions have suggested that tides are related to earthquake swarm activities associated with crustal fluids. Therefore, we investigated whether tides are also involved in the Noto earthquake swarm activity. Our results suggest a tidal correlation only at greater depths in the southern part of the analyzed area ('region Sd'). There, we inferred that an increase in pore fluid pressure caused by the inflow of deep fluids may have led to a decrease in fault fracture strength, making the local seismicity relatively susceptible to the effects of tidal forces. The significantly high value in region Sd of the scaling parameter  $b$  of the Gutenberg–Richter law (describing the earthquake magnitude–frequency distribution) and observed crustal deformation are consistent with this interpretation.

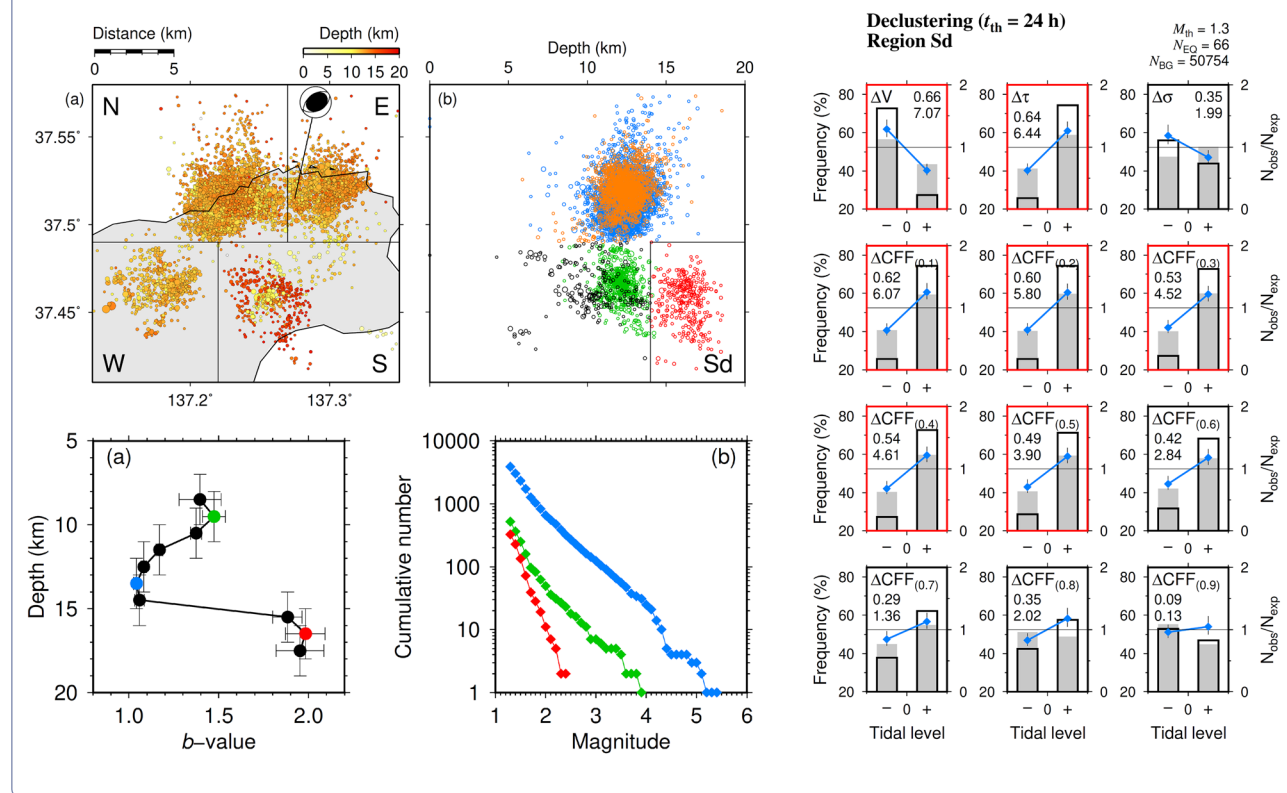
**Keywords** Tide, Noto region, Earthquake swarm, Crustal fluids, Gutenberg–Richter law

\*Correspondence:

Fuyuki Hirose  
fhirose@mri-jma.go.jp

Full list of author information is available at the end of the article

## Graphical Abstract



## Introduction

In the Noto region of Japan, increased seismicity has persisted since around 2018, with the area of seismicity broadening in December 2020 and further still in July 2021 (Japan Meteorological Agency (JMA) 2023a). Additionally, crustal deformation (expansion and uplift) has been observed there since around the end of 2020 (Nishimura et al. 2023). The presence of crustal fluids has been suggested as a factor behind this swarm activity (Nakajima 2022; Amezawa et al. 2023). Elsewhere, the well-known Matsushiro earthquake swarm activity that started in 1965 was similarly attributed to crustal fluids (e.g., Yoshioka et al. 1970; Ohtake 1974; Yoshida et al. 2002), as well as to tides (e.g., Iwata and Nakanishi 1998). Miguelanz et al. (2021, 2023) examined the behavior of magma in the Canary Islands based on the relationship between earthquake swarms in volcanic areas and tides. Han et al. (2018) examined the relationship between deep long-period earthquakes associated with magmatic and/or fluid behavior beneath Mt. St. Helens and tidal stresses, finding a correlation with compressional volumetric tidal stress. Further investigation of the relationship between seismic swarm activity and tides may therefore help elucidate the mechanism(s) behind seismic

swarm activity. Therefore, in this study, we analyzed the relationship between earthquake swarm activity and tides in the Noto region.

## Data

The earthquake swarm activity in the Noto region can be spatially divided into four clusters in the northern, southern, eastern, and western areas (regions N, S, E, and W, respectively) (Fig. 1a). Furthermore, in region S, activity can be divided into two depth clusters: Ss (hypocenters shallower than 14 km) and Sd (deeper than 14 km) (Fig. 1b). Thus, we examined five clusters of earthquake swarm activity: regions N, Ss, Sd, E, and W. From the JMA unified hypocenter catalog, we extracted 6,202 high-precision hypocenters of events with magnitude  $M \geq 1.3$  (Fig. 1c) and flags K, k, or A (where K indicates a fully reviewed hypocenter, k a simply reviewed hypocenter, and A an automatically processed hypocenter; see JMA 2023b for details) occurring between 1 January 2018 and 31 December 2022 in the area within 37.41–37.58°N and 137.13–137.35°E (Fig. 1a) and at hypocenter depths of less than 20 km.

Several methods for estimating the threshold magnitude  $M_{th}$  have been proposed (Woessner and Wiemer

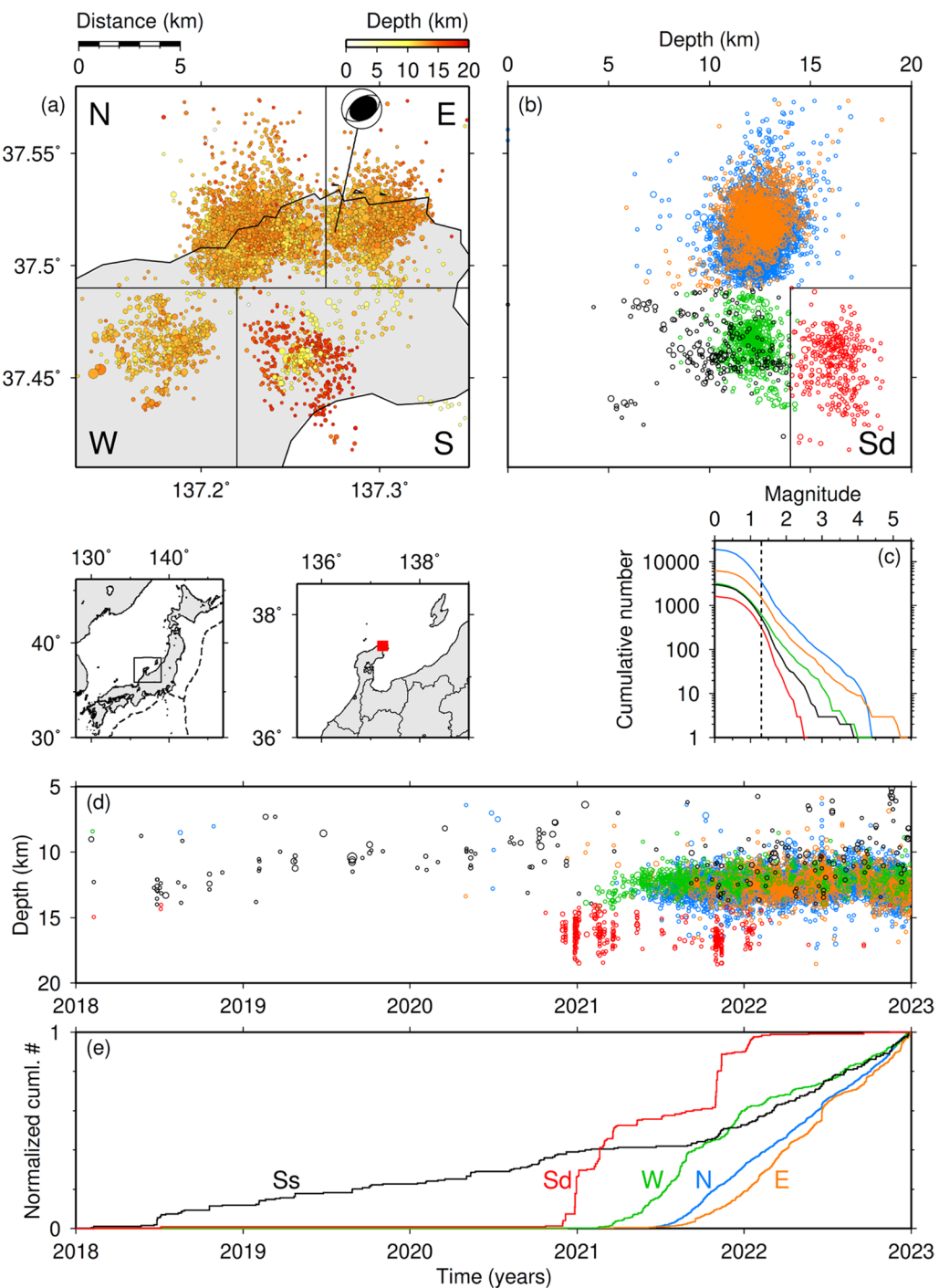


**Fig. 1** Study area and hypocenter distribution. **a** The four regions of earthquake swarm activity (regions N, S, E, and W) based on the epicentral distribution of earthquakes in the study area with flags of K, k, or A, hypocentral depths shallower than 20 km, and magnitudes of  $M \geq 1.3$  or higher occurring between 1 January 2018 and 31 December 2022 extracted from the JMA unified hypocenter catalog. The color scale shows hypocentral depth, and symbol size is proportional to  $M$ . The JMA CMT solution for the largest earthquake ( $M 5.4, M_w 5.1$ ), which occurred in region E on 19 June 2022, is also shown. The outsets show the location of the study area (red) on wider area maps. **b** Hypocenters projected onto a north–south cross section. Region S is divided into shallow (Ss) and deep regions (Sd). Symbol colors correspond to regions N (blue), E (orange), W (green), Ss (black), and Sd (red). **c** Cumulative frequency–magnitude distribution. The vertical dashed line indicates the threshold magnitude  $M_{th} = 1.3$ . **d** Time series of hypocentral depths. **e** Time series of the cumulative number of earthquakes normalized by the total number of earthquakes in each region (3528, 1521, 630, 203, and 320 in regions N, E, W, Ss, and Sd, respectively). Symbol colors in **c–e** are the same as in **b**.

2005): For example, the MAXC method (Wiemer and Katsumata 1999) define magnitude with the maximum curvature of the frequency–magnitude distribution as  $M_{\text{th}}$ , and this generally matches the magnitude bin with the highest frequency of events in the non-cumulative frequency–magnitude distribution (Woessner and Wiemer 2005). Another method, the EMR method (Woessner and Wiemer 2005), estimates  $M_{\text{th}}$  based on the Gutenberg–Richter (G–R) law (Gutenberg and Richter 1944) using the entire data set, including the range of magnitudes reported incompletely. On average,  $M_{\text{th}}$  determined by the EMR method corresponds to  $M_{\text{th}}$  determined by the MAXC method plus 0.2. In each region analyzed in this study, the magnitude of bin with the highest frequency of events (that is, corresponding to  $M_{\text{th}}$  of the MAXC method) ranges from 0.6 to 0.9, corresponding to 0.8 to 1.1 of  $M_{\text{th}}$  of the EMR method. We also visually confirmed the shape of the frequency–magnitude distribution, and to be on the safe side, adopted 1.3 as  $M_{\text{th}}$  common to each region (Fig. 1c).

During this period, the number of earthquakes first began to increase in region Ss in mid-2018, region Sd became seismically active in December 2020, and the activity then expanded to regions W, N, and E in 2021 (Fig. 1d, e). The largest earthquake ( $M$  5.4) occurred in region E on 19 June 2022 and was produced a maximum seismic intensity of 6 Lower on the JMA Seismic Intensity Scale (<https://www.jma.go.jp/jma/en/Activities/inttable.html>). We note that on 5 May 2023 (after our analysis period), a larger earthquake of  $M$  6.5 (maximum seismic intensity 6 Upper) occurred in region E, and the subsequent expansion of the active region in the ocean area has blurred the boundary between regions N and E. Added on February 8, 2024: after the paper was submitted (December 11, 2023), on January 1, 2024,  $M$  7.6 earthquake (maximum seismic intensity 7) occurred with the rupture starting point at 37.5°N near the boundary between regions N and E.

Calculation of theoretical tidal responses requires the hypocentral location, occurrence time, and fault parameters. For the hypocentral location and occurrence time, we used catalog information. For the fault parameters, we assumed that reverse faults with a northeasterly strike and southeasterly dip predominated (i.e., we assigned to all events a strike of 45°, a dip of 45°, and a rake of 90°). This is consistent with the regional tectonic stress field (Terakawa and Matsu'ura 2022), the focal mechanisms of major earthquakes, and the hypocentral distribution (Amezawa et al. 2023).

## Method

### Theoretical tidal response

We calculated theoretical tidal responses on the faults using the “TidalStrain.2” Fortran software (Hirose et al. 2019). We investigated changes in the following 12 components as tidal indices: volume strain  $\Delta V$  at the hypocenter, shear stress  $\Delta \tau$ , normal stress  $\Delta \sigma$ , and the Coulomb failure function  $\Delta \text{CFF} = \Delta \tau + \mu' \Delta \sigma$  for assumed apparent friction coefficients  $\mu'$  of 0.1, 0.2,..., 0.9 (denoted  $\Delta \text{CFF}_{(0.1)}$ ,  $\Delta \text{CFF}_{(0.2)}$ ...,  $\Delta \text{CFF}_{(0.9)}$ , respectively) on the assumed fault plane. If a highly anisotropic fault hosted fluid-filled fractures aligned along the fault zone,  $\mu' = \mu_0(1 - B)$  (Houston 2015), where  $\mu_0$  is the static friction coefficient and  $B$  is Skempton's coefficient, which indicates the ratio of the change in pore fluid pressure to the change in confining pressure acting on the rock under undrained conditions. Accordingly, if the response of pore pressure to  $\Delta \sigma$  is strong (i.e.,  $B \sim 1$ ) at the fault plane,  $\mu'$  becomes small and the contribution of  $\Delta \tau$  to  $\Delta \text{CFF}$  becomes dominant. In the case of  $\Delta V$  and  $\Delta \sigma$ , we defined expansion/dilatation as positive and contraction/compression as negative, and we defined  $\Delta \tau$  and  $\Delta \text{CFF}$  as positive when they promoted fault slip. We assigned phase angles of  $-180^\circ$  and  $+180^\circ$  to the local tidal minima before and after an event, respectively, and  $0^\circ$  to the tidal maximum between these two local minima. The phase angle  $\psi$  at the earthquake occurrence time was estimated by linear interpolation over the time interval between  $-180^\circ$  and  $0^\circ$  or between  $0^\circ$  and  $+180^\circ$  (Fig. 2). The tidal level  $L$  at the earthquake occurrence time was defined as the strain or stress value with a positive or negative sign relative to the zero line.

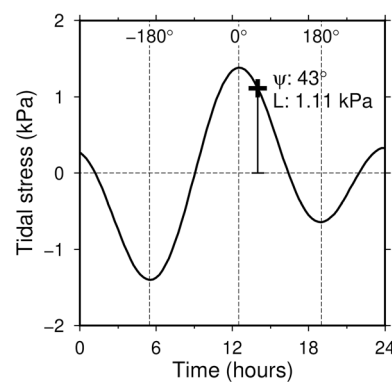


**Fig. 2** Example of temporal change in tidal stress. Example of changes in tidal stress in relation to time (black curve) and the estimated phase angle  $\psi$  and tidal level  $L$  at the earthquake occurrence time (cross)

### Sensitivity to tidal phase angle: Schuster test

The possibility of earthquakes occurring at a particular tidal phase angle is commonly evaluated by using the *p*-value (Schuster 1897), calculated as follows:

$$p = \exp\left(-\frac{D^2}{N}\right), \quad (1)$$

$$D^2 = \left(\sum_{i=1}^N \cos \psi_i\right)^2 + \left(\sum_{i=1}^N \sin \psi_i\right)^2, \quad (2)$$

where  $N$  is the total number of earthquakes,  $\psi_i$  is the phase angle at the occurrence time of the  $i$ th earthquake. An approximation of Eq. (1) is sufficient when  $N$  is larger than 10 (Heaton 1975). The *p*-value (which ranges from 0 to 1) represents the significance level for rejecting the null hypothesis that earthquakes occur randomly with respect to the tidal phase angle, such that the confidence that the null hypothesis is rejected is greater when the *p*-value is smaller. In general, *p*-values of 0.05 (Tanaka et al. 2002) are used to judge tidal correlations.

If the occurrence of an earthquake is influenced by tides, there should be a peak in tidal phase angle histograms near a phase that promotes fault slip (for example, ΔCFF of 0°). Therefore, we fit a sinusoidal curve  $\Psi(\psi)$  to the frequency distribution of tidal phase angles as follows:

$$\Psi(\psi) = A_0 + A_1 \cos(\psi - \psi_p), \quad (3)$$

where  $A_0$  is the mean relative frequency, fixed at 8.333% (=1/12 of 100%) for the adopted phase angle bin width of 30°, and  $A_1$  and  $\psi_p$  are the amplitude and phase, respectively, of the least-squares-fitted curve.  $\psi_p$  becomes significant only when  $p$  is small because larger *p*-values suggest lower correlations with tides. In addition, when a peak appears at times when fault slip is suppressed, it is physically reasonable to infer a spurious correlation.

### Sensitivity to tidal level: Houston plot

We also investigated the dependence of an earthquake on the tidal level (amplitude). An example is shown in Fig. 3. As a first step, we investigated the case that the tidal level is divided into two bins, positive or negative (Fig. 3b), because if the number of earthquakes in each bin is small and the number of bins is large, the estimation error becomes large and meaningful results cannot be obtained. The tidal sensitivity in this case can be simply defined as the absolute value of the difference between the  $N_{\text{obs}}/N_{\text{exp}}$  ratios in the two bins (corresponding to the slope of the blue line in Fig. 3b), where  $N_{\text{obs}}$  is the number of earthquakes observed during the period when the tidal force takes the value within the strain/stress bin (i.e., positive or negative), and  $N_{\text{exp}}$  is the expected number of earthquakes in the same period if there were no correlation to tides (here  $N_{\text{exp}}$  is based on

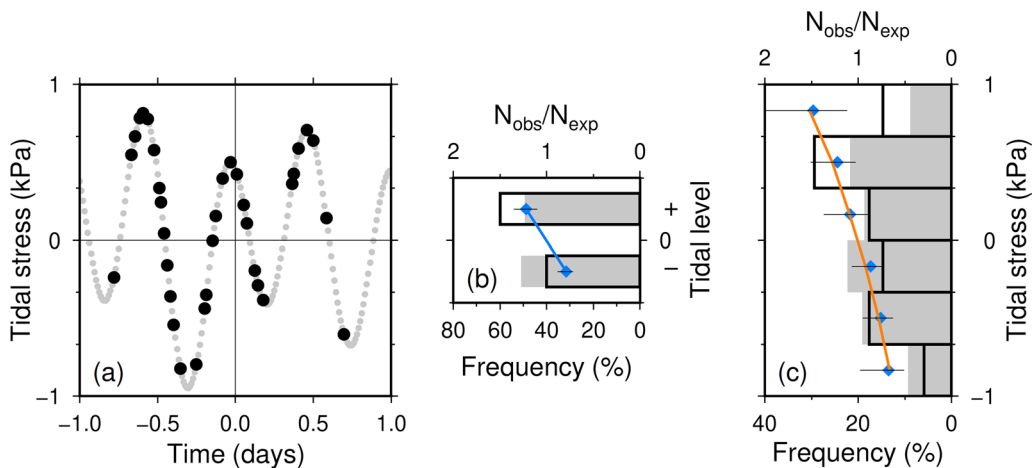


**Fig. 3** Example of Houston plot. **a** Theoretical tidal response (gray circles, sampling interval 15 min). Black circles indicate earthquake occurrences. **b** Example of a Houston plot in which the tidal stress is divided into two bins: positive or negative. The gray bars show the distribution of the expected background relative frequency  $N_{\text{exp}}$  of tidal stress (relative frequency distribution of tidal stress during 1 day before and 1 day after the earthquake, sampling interval 15 min), and the bars outlined by thick black lines show the distribution of the relative frequency  $N_{\text{obs}}$  of tidal stress at the time of the earthquake (bottom axis). The error bars show the  $1\sigma$  error (assuming a total of 100 events), where  $\sigma = \sqrt{np_i(1-p_i)}$  for the binomial distribution  $B(n, p_i)$ ,  $n$  is the total number of earthquakes, and  $p_i$  is the probability of random events in the  $i$ th bin obtained from the frequency distribution of theoretical tidal values. The blue diamonds, which show the ratio of  $N_{\text{obs}}$  to  $N_{\text{exp}}$  (top axis), are connected by a straight blue line. **c** Example of a Houston plot in which the tidal stress is divided into six bins. The orange line indicates the value obtained by maximum likelihood method (Yabe et al. 2015) of  $N_{\text{obs}}(\Delta S)/N_{\text{exp}}(\Delta S) = e^{\alpha \Delta S}$  (Eq. (4)) to the  $N_{\text{obs}}/N_{\text{exp}}$  values in the six bins. In this example, tidal sensitivity  $\alpha = 0.5$

the tidal amplitude sampled at 15-min intervals during 4 days before and after each earthquake). To test whether a correlation was statistically significant, we used a Chi-square test at a significance level of 5% to test the null hypothesis that the event occurrence rate and the tidal occurrence rate (background distribution) belong to the same population.

If the first step suggested a correlation between earthquakes and tides, we proceeded to the second step. To evaluate whether the likelihood of an earthquake increases as the tidal level increases, we used the following formula (Houston 2015) for the case that the tidal level is subdivided into six bins (Fig. 3c):

$$N_{\text{obs}}(\Delta S)/N_{\text{exp}}(\Delta S) = e^{\alpha \Delta S}, \quad (4)$$

where  $\Delta S$  is the intermediate value in a strain or stress bin, and  $\alpha$  represents tidal sensitivity. If the ratio  $N_{\text{obs}}/N_{\text{exp}}$  (blue diamonds in Fig. 3c) of the frequency distribution of tidal values at the time of an earthquake's occurrence is proportional to the tidal stress, then a relationship with the tide is indicated. A Chi-square test with a significance level of 5% was used to test the statistical significance of the correlation. In this study, we refer to plots such as those illustrated in Fig. 3b, c as 'Houston plots.'

### Declustering method

When an earthquake occurs, earthquakes such as aftershocks are likely to be induced in the surrounding area as a result of stress redistribution. When the tidal correlation of seismic activity is investigated, if such aftershocks are not excluded (i.e., declustered) in advance, apparently high tidal correlations tend to appear (Nagata et al. 2022). In general, declustering is a process that extracts independent events by excluding earthquakes that occurred closely in space and time. In this study, we analyzed data obtained by using a general declustering method (e.g., De Natale and Zollo 1986).

We applied this declustering method as follows: in each region, a series of earthquakes in which the time interval between successive earthquakes was within the threshold time  $t_{\text{th}}$  was considered to be one group, and all but the first earthquake in each group were excluded. To obtain the declustered catalog, we performed a Kolmogorov–Smirnov test with the significance level set to 5% using the frequency distribution of the time intervals between consecutive earthquakes and the theoretical time interval for a stationary Poisson process. We finally adopted a minimum value of  $t_{\text{th}}$  of 1, 2, 3, 4, 5, 6, 12, 24, 48, 72, 96, or 120 h if the null hypothesis "the time series after declustering is a stationary Poisson process" could not be rejected.

When the test period was set to the entire study period (1 January 2018 to 31 December 2022), there was no value of  $t_{\text{th}}$  in any region for which the null hypothesis could not be rejected (note that the null hypothesis was rejected when the test period was the entire study period because the predominant occurrence interval was significantly different between the period of normal activity and the swarm period). Therefore, we limited the test period to the swarm period in each region (rightmost column of Table 1), defined as the period after a distinct change in slope was observed in the cumulative seismicity trend (Fig. 1e). To obtain the declustered catalog, we then determined the  $t_{\text{th}}$  value for which the null hypothesis could not be rejected in each region (Table 1). Note that when we applied declustering using the determined  $t_{\text{th}}$  values (Table 1) to data from other periods in each region, we were able to confirm by a Kolmogorov–Smirnov test that the null hypothesis could not be rejected except in region N. Because in region N, however,  $t_{\text{th}}$  was 48 h (that is, the interval between earthquakes in the declustered catalog was longer than the durations of the principal tidal cycles of ~12 and 24 h), we inferred that the declustered catalog obtained in region N would not affect the evaluation of tidal correlation. Therefore, in subsequent analyses, we used declustered data for the entire period for each region (Table 1).

## Results and discussion

### Sensitivity to tidal phase angle

Tidal phase angle–frequency histograms for each region and each tidal index are shown in Fig. 4. We obtained statistically significant tidal correlations in regions Ss and Sd (i.e.,  $p < 0.05$  in the Schuster test). However, in region Ss, the peak phase angle  $\psi_p$  is approximately +90°; by definition, slip begins to be

**Table 1** Declustering results

Region	# of events		$t_{\text{th}}$ (h)	Test period (swarm period) (yyyy/mm/dd)
	Original	After declustering		
N	3528	7 (19)	48	2021/6/1–2022/12/31
E	1521	32 (45)	48	2021/8/1–2022/12/31
W	630	26 (28)	120	2021/2/1–2022/12/31
Ss	203	95 (156)	12	2021/9/1–2022/12/31
Sd	320	60 (66)	24	2020/11/1–2022/2/28

Number of events for which the null hypothesis that 'declustered seismic activity is a stationary Poisson process' could not be rejected at the significance level of 5% after the declustering method was applied to events during the swarm period (i.e., declustering was successful). The numbers in parentheses, which show the number of earthquakes remaining after the declustering method was applied to the entire period (1 January 2018 to 31 December 2022), were used in this analysis

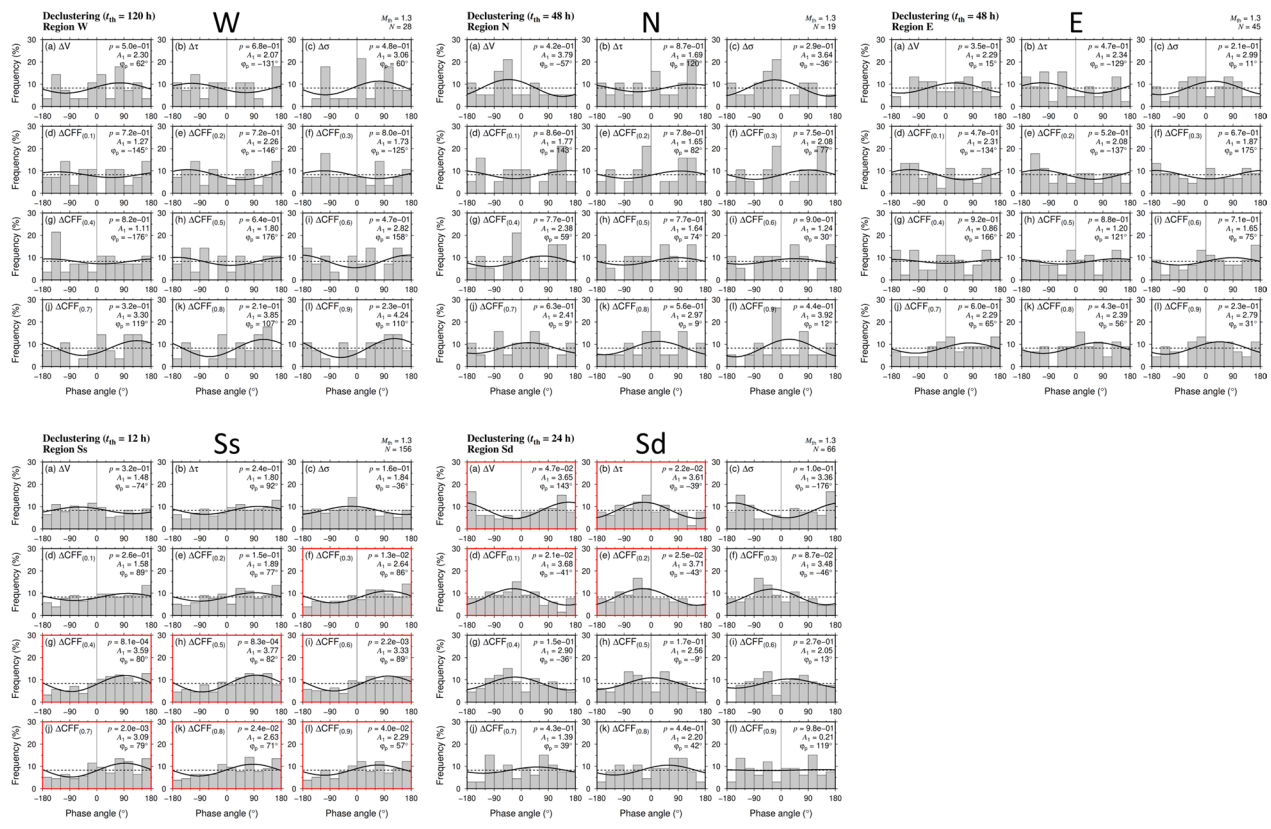


**Fig. 4** Tidal phase angle histograms for each tidal index in each of the five regions. For each region, the number of earthquakes  $N$  is shown at the top right (above panel c). The dashed line in each panel shows the average relative frequency, and the thick curve is the sine wave approximation with amplitude  $A_1$  and peak phase angle  $\varphi_p$ . Cases with significant correlations ( $p < 0.05$ ) are framed in red

suppressed at this phase angle. According to the Dieterich model (Dieterich 1994), which is based on the rate-and state-dependent friction constitutive law, the peak of seismicity rate may appear delayed from the peak of the stressing rate. For example, in Nakata et al. (2008), which investigated the relationship between deep tectonic tremors and tides in eastern Shikoku, a peak difference of about 1–2 h was observed. Regarding region Ss, there was a delay of about 180°, or about 6 h on average, from the peak of stressing rate (tidal phase angle of  $-90^\circ$ ) to the peak of the number of earthquakes ( $90^\circ$ ). We preliminarily input a 12-h periodic sinusoidal wave that simulates the tidal stressing rate into the Dieterich model and performed calculations by changing several parameter values, but the maximum delay was only 3 h. Therefore, tidal correlations for region Ss are questionable. In region Sd, we obtained significant tidal correlations for  $\Delta V$ ,  $\Delta\tau$ ,  $\Delta CFF_{(0.1)}$ , and  $\Delta CFF_{(0.2)}$ . The peak phase angle  $\psi_p$  of  $\Delta V$  of  $\sim +140^\circ$  indicates that earthquakes tended to occur during volumetric contraction. The peak phase angles  $\psi_p$  of  $\Delta\tau$ ,  $\Delta CFF_{(0.1)}$ , and  $\Delta CFF_{(0.2)}$ , all  $\sim -40^\circ$ , indicate that earthquakes tended to occur at times when tidal stress accelerated fault slip.

Figure 5 shows the relationship of the tidal phase angles between pairs of the four tidal indices in region Sd for which a tidal correlation was indicated. Almost no phase difference exists between  $\Delta\tau$  and  $\Delta CFF_{(0.1)}$  or  $\Delta CFF_{(0.2)}$  (Fig. 5e, f) or between  $\Delta CFF_{(0.1)}$  and  $\Delta CFF_{(0.2)}$  (Fig. 5c), whereas the phase difference between  $\Delta V$  and the other indices was  $\sim 180^\circ$  (Fig. 5a, b, d). The Schuster test is sensitive to bias in the phase angle distribution but returns similar  $p$ -values for samples with a definite phase difference. Therefore, these four tidal indices are inferred to show the same degree of tidal correlation.

Because the  $p$ -value of  $\Delta CFF_{(0.1)}$  was the smallest among these four indices,  $\Delta CFF_{(0.1)}$  may be the tidal index that controls earthquake swarm activity. However, because the actual fault shape may differ from the assumed fault parameters, the dominance of this index cannot be determined here. Previous studies (Fig. 7c of Japan Meteorological Agency 2023a and Fig. 1 of Amezawa et al. 2023) show focal mechanism solutions (P-wave first-motion polarity solution, CMT solution, and NIED MT solution) for the Noto earthquake swarm activity, and show that the reverse-fault event with fault parameters assumed in this study are dominant. However,

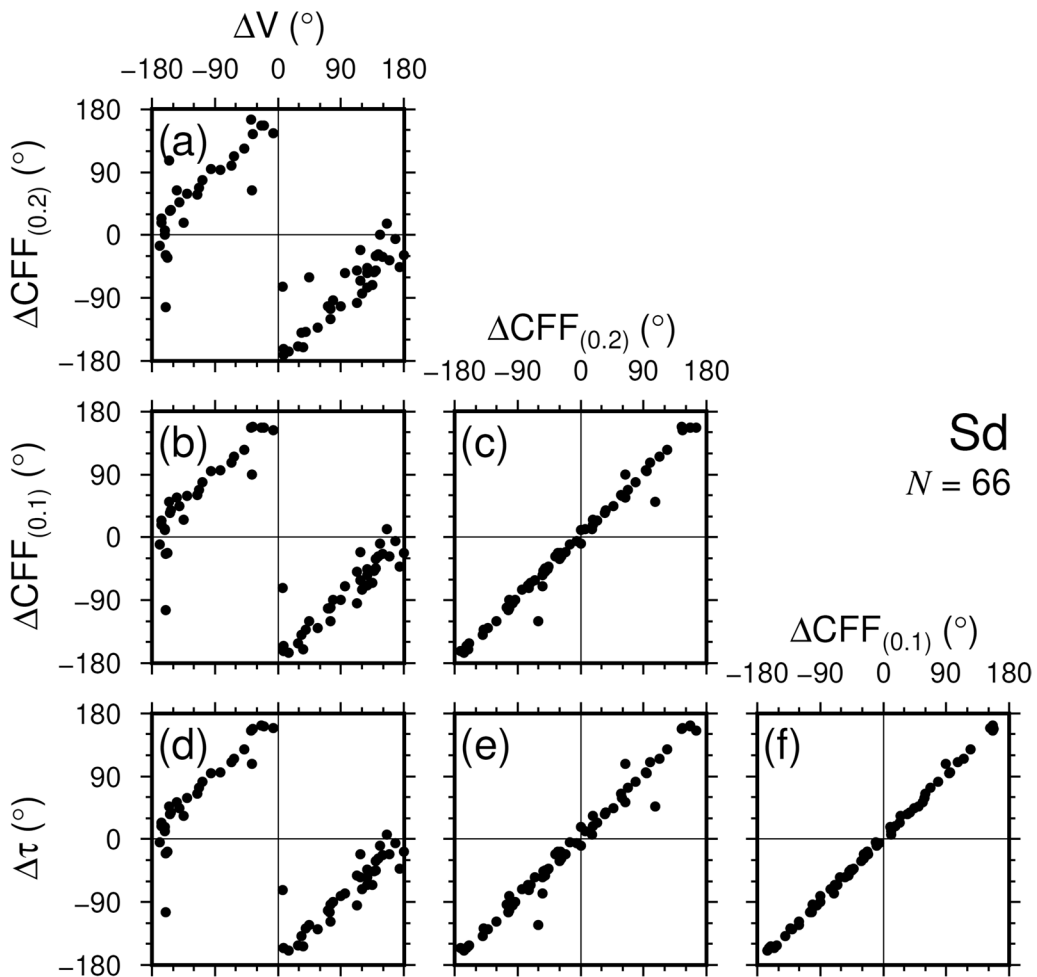


**Fig. 5** Relationships of tidal phase angles between pairs of the four significant tidal indices in region Sd.  $\Delta\tau$  and  $\Delta\text{CFF}_{(0.1, 0.2)}$  each show a phase difference of  $\sim 180^\circ$  with respect to  $\Delta V$

the events for which focal mechanisms have been estimated are mainly in regions N and E, and for events with  $M < 3.2$ , even the P-wave first-motion polarity solution has not been determined (note that focal mechanisms for all events with  $M \geq 3.2$  are not determined). Therefore, it is unclear whether focal mechanisms of small earthquakes are consistent with the assumed fault parameters. Nonetheless, because a tidal correlation is indicated even for  $\Delta V$ , which does not depend on fault parameters, at minimum it can be inferred that the earthquake swarm activity in region Sd is influenced by tides.

#### Sensitivity to tidal level

Figure 6 shows Houston plots for the case of two bins, positive and negative. The tidal sensitivity, that is, the degree of deviation from the background distribution (indicated by the slopes of the blue lines in Fig. 6), is greater in region Sd than in the other regions. In region Sd, significant tidal correlations are indicated for  $\Delta V$ ,

$\Delta\tau$ , and  $\Delta\text{CFF}_{(0.1-0.5)}$  (red frames in Fig. 6). Although the Chi-square value for  $\Delta V$  was largest among the seven indices, it is not possible to determine which tidal index controls earthquake swarm activity (see “[Sensitivity to tidal phase angle](#)”). No relationship with tides is suggested for earthquakes in the other regions.

Figure 7 shows the relationships between tidal phase angle and tidal level, as indicated by tidal indices  $\Delta V$ ,  $\Delta\tau$ , and  $\Delta\text{CFF}_{(0.1, 0.2)}$  in region Sd. Tidal levels are generally positive for phase angles from  $-90^\circ$  to  $+90^\circ$  and generally negative for other phase angles. Therefore, the tidal components suggesting a tidal correlation in the Houston plots with two bins and those suggested by the Schuster test results (“[Sensitivity to tidal phase angle](#)”) are mostly the same. Because tidal levels were not necessarily negative when the tidal phase angle was outside of the  $-90^\circ$  to  $+90^\circ$  range, the Schuster test results did not suggest any correlation with  $\Delta\text{CFF}_{(0.3-0.5)}$ .

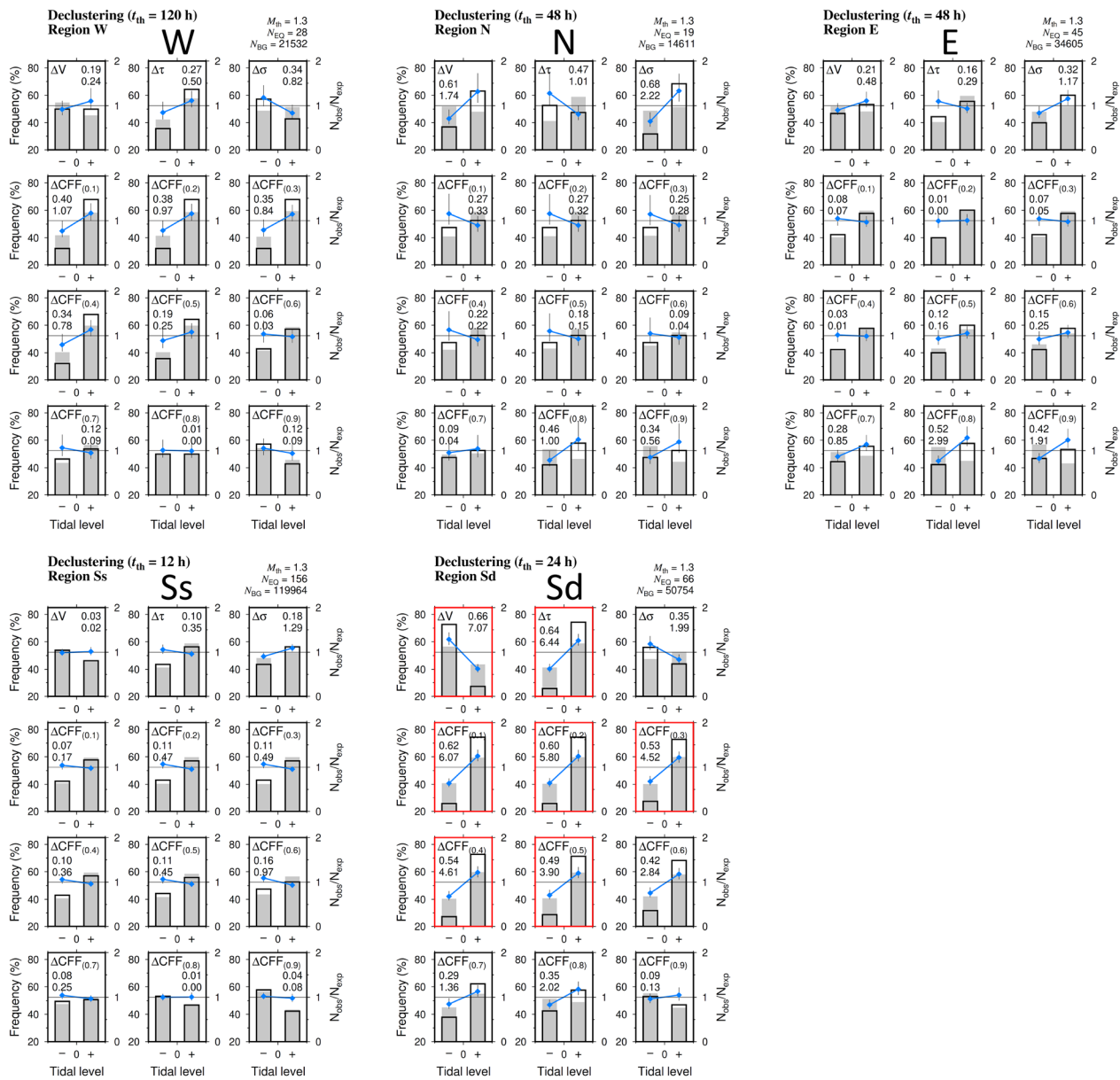


**Fig. 6** Houston plots with two bins, positive and negative, for each tidal index in each region. See Fig. 3b for how to read the figure. For each region, the number of earthquakes  $N_{EQ}$  meeting the threshold magnitude  $M_{th}$  of 1.3 is shown along with  $N_{BG}$  which is the number sampled at 15-min intervals during four days before and four days after each earthquake,  $N_{BG} = 769 \times N_{EQ}$ . The first value in each panel is the absolute value of the difference between the  $N_{obs}/N_{exp}$  ratios in the two bins (corresponding to the slope of the blue line); the slope becomes greater as the event occurrence distribution deviates from the background distribution. The second value in each panel is the Chi-square value. In panels showing a Chi-square value of 3.8415 or higher (framed in red), the null hypothesis is rejected at a significance level of 5%

Next, to gain a more detailed understanding of the trends in region Sd, we examined Houston plots for the case of 6 bins (Fig. 8). These frequency distributions, which show the same tendencies as those with two bins (Fig. 6), also suggest a correlation with tides. However, in no case could the null hypothesis be rejected at

the 5% significance level based on the Chi-square test result.

To summarize, although it cannot be said that an earthquake is more likely to occur when the tidal level is larger, the Houston plots in region Sd indicate a tidal correlation. It is not possible to determine, however, which tidal

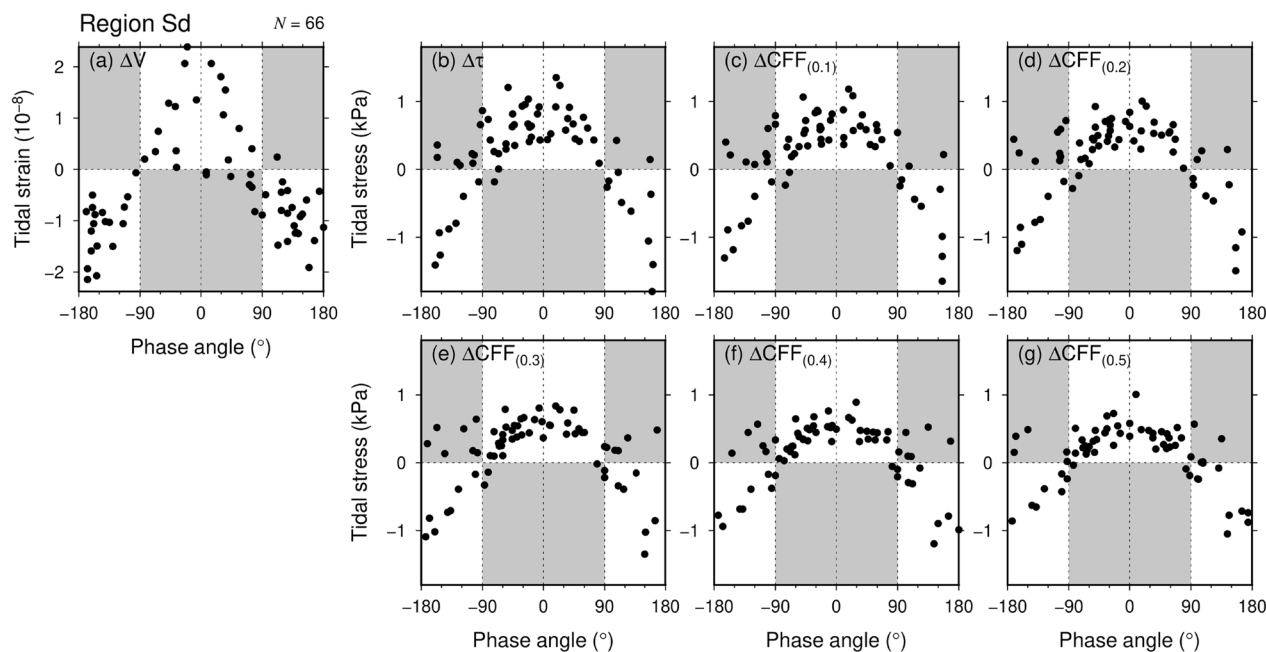


**Fig. 7** Relationship between tidal phase angle and the seven dominant tidal level indices in region Sd. **a**  $\Delta V$ , **b**  $\Delta \tau$ , **c**  $\Delta CFF_{(0.1)}$ , **d**  $\Delta CFF_{(0.2)}$ , **e**  $\Delta CFF_{(0.3)}$ , **f**  $\Delta CFF_{(0.4)}$ , and **g**  $\Delta CFF_{(0.5)}$ . When the phase angle was in the range of  $-90^\circ$  to  $+90^\circ$ , the tidal level was generally positive, and generally negative otherwise (white areas in each panel). However, there were some exceptional events that fall into the gray area

index is dominantly associated with the triggering of earthquakes.

#### Spatial distribution of the *b*-value of the Gutenberg–Richter law

The G–R law,  $\log N = a - bM$ , describes the earthquake magnitude–frequency distribution, and its *b*-value is a scaling parameter. The *b*-value was estimated using the maximum likelihood method (Utsu 1965; Aki 1965),  $b = \log_{10} e / (\bar{M} - M_{th})$ , where  $\bar{M}$  is the average magnitude. The uncertainty of *b*-value was calculated from  $\sigma = b / \sqrt{N}$  derived by Aki (1965). Table 2 shows the G–R *b*-values for the entire study area and within each region. For earthquakes in region Sd with hypocentral depths below 14 km, the *b*-value was 1.85, considerably larger than those in the other four regions ( $\sim 1.1$ ) as well as the median value for all of Japan ( $\sim 0.9$ ; Nagata et al. 2022). Over the entire analyzed region, the *b*-value tends to gradually decrease from a depth of 10 km to 14 km, and below that depth it increases (Fig. 9a).

Spada et al. (2013) investigated depth changes in the G–R *b*-value for earthquakes occurring in continental crust around the world, and found that the *b*-value decreases with depth to about 15 km (about 25 km in Switzerland), and then increases below that depth. They indicated that the depth dependence of the *b*-value is due to the strength profile (differential stress dependence) of the continental crust, and that the inflection point, i.e.,

the depth at which the *b*-value begins to increase, corresponds to the brittle–ductile transition in the crust. Because the brittle–ductile transition depth beneath the Noto region of Japan is  $\sim 13$  km (the D90 depth; Omurallieva et al. 2012), the depth dependence of the *b*-value obtained here is generally consistent with the differential stress dependence reported by Spada et al. (2013). However, the average *b*-value in Japan at 15–20 km depth, i.e., after the *b*-value begins to increase below the brittle–ductile transition, is only about  $0.85 \pm 0.05$  (Spada et al. 2013); thus, the *b*-value of  $2.0 \pm 0.1$  (Fig. 9a) in this depth range in the Noto region is uniquely high.

High *b*-values are often observed around magma chambers, for example, in the active seismic swarm area off Ito on the Izu Peninsula (Wyss et al. 1997) and directly beneath volcanoes in the Tohoku region (Wyss et al. 2001). Because areas around magma chambers are highly fractured and hot (Wyss et al. 1997) and/or under a low stress field due to high pore fluid pressure (Wyss et al. 2001), it has been interpreted that large fractures cannot occur around magma chambers; as a result, the slope of the earthquake magnitude frequency distribution is high (i.e., the G–R *b*-value is high).

In region Sd, observations of hypocenter migration (Amezawa et al. 2023) and crustal deformation (Nishimura et al. 2023) suggest that high-pressure fluids are supplied from depth, and a tomographic analysis has suggested that beneath the Noto Peninsula,

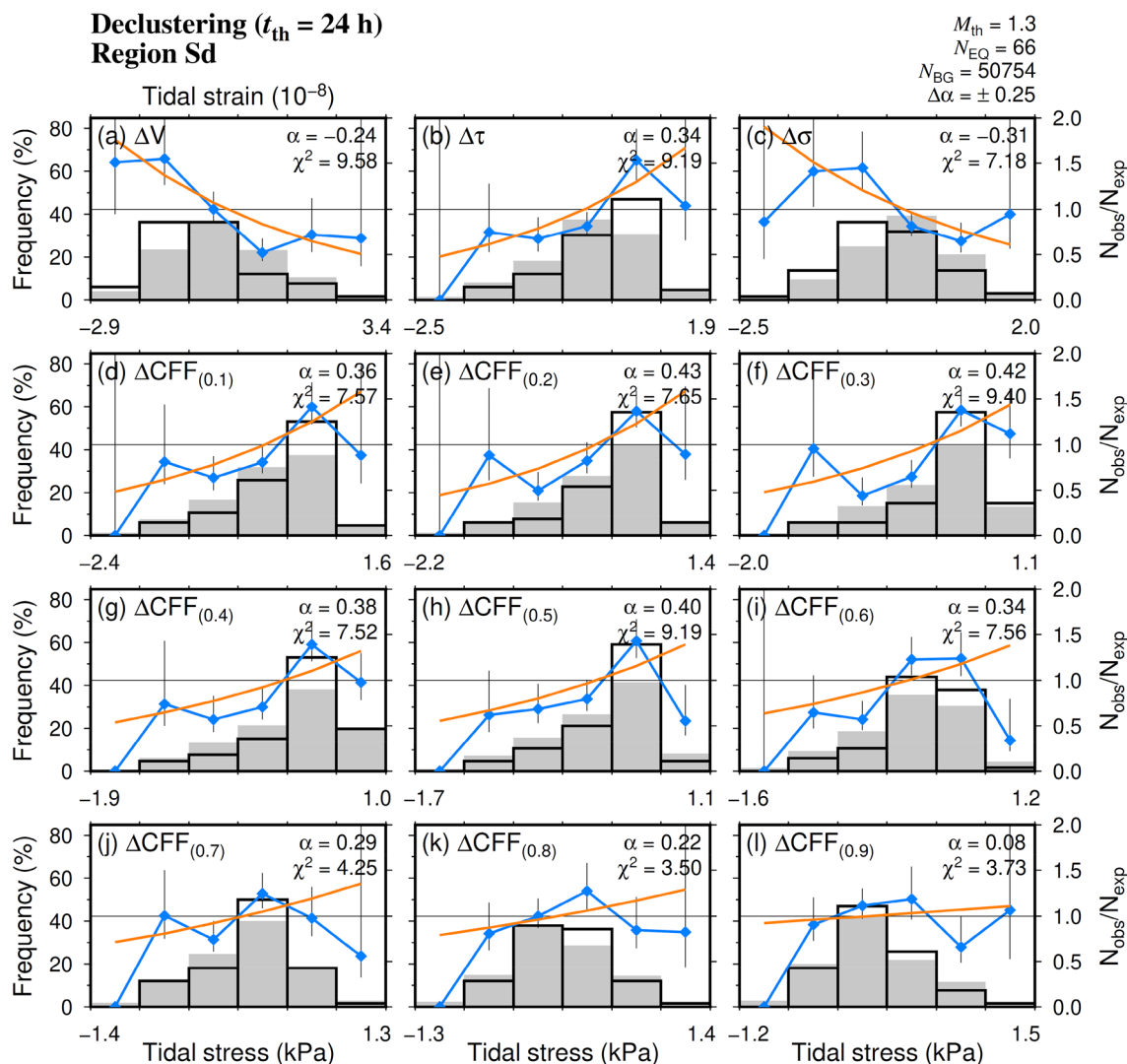


**Fig. 8** Houston plots with six bins for each tidal index in region Sd. See Fig. 3c for how to read the figure. The horizontal axis shows the minimum-to-maximum range of each index. In no cases could the null hypothesis be rejected at the 5% significance level based on the Chi-square test. Bins with  $N_{\text{obs}} = 0$  have error bars of zero length.  $\Delta\alpha$  represents the uncertainty in the estimated parameter  $\alpha$  and corresponds to the 95% confidence interval of a Gaussian distribution (Yabe et al. 2015)

fluids originating from the mantle are being supplied to the lower crust (Nakajima 2022). In addition to the tendency toward increased  $b$ -values at greater depths,

high-pressure fluids may be responsible for the uniquely high  $b$ -values in region Sd.

**Table 2**  $b$ -value of the G-R law

Region	$N$	$b$	$\sigma$
All	6196	1.16	0.02
N	3528	1.16	0.02
E	1521	1.10	0.03
W	630	1.11	0.04
Ss	203	1.12	0.08
Sd	320	1.85	0.10

$N$  is the total number of events

#### Possible explanation for the high tidal correlation in region Sd

Taken together, our results suggest that the high tidal correlation in region Sd results from the following:

1. In region Sd, the deeper hypocenters and higher  $b$ -values than in the other regions suggest that the differential stress in region Sd is small, based on the previously reported depth distribution of  $b$ -values (Spada et al. 2013).

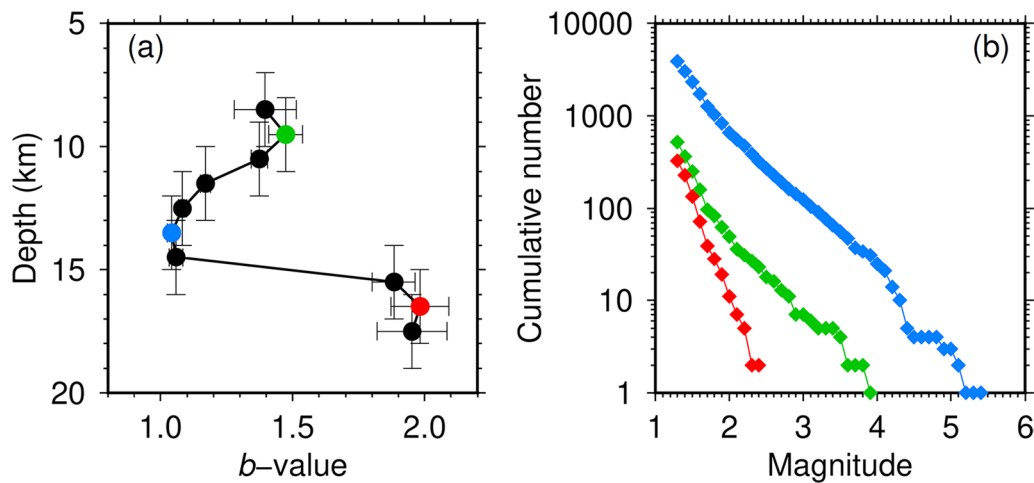


**Fig. 9** Depth change of *b*-value. **a** Change of the *b*-value with depth in the Noto region. The vertical bars show the depth range used to estimate each *b*-value, and the horizontal bars show the  $1\sigma$  error. The symbol colors correspond to **b** cumulative frequency–magnitude distributions at selected depths

2. The results of studies on hypocenter migration (Amezawa et al. 2023), crustal deformation (Nishimura et al. 2023), and tomography (Nakajima 2022) in the Noto region suggest that high-pressure fluids may be present in region Sd, which in turn suggests that the fracture strength is lower in region Sd than in the other regions because of the increased pore fluid pressure.
- The uniquely high *b*-value of region Sd reflects the effects of both (1) and (2).
- If high-pressure fluid is present in region Sd, then fault strength is likely affected by fluctuations in pore fluid pressure caused by tidal volume changes.

The low rupture strength in region Sd can be considered to make the region more susceptible to tidal influence; thus, seismic activity in region Sd is more affected by tidal fluctuations than that in the other regions.

## Summary

The relationship between earthquake swarm activity and tides in the Noto region was evaluated by using the Schuster test (sensitivity to tidal phase angle) and Houston plots (sensitivity to tidal level). A tidal correlation was indicated only at depth in the south of the study area ('region Sd'). The dominant tidal indices were  $\Delta V$ ,  $\Delta \tau$ , and  $\Delta CFF$  (with small  $\mu'$ ), but the strongest among these could not be determined.

In region Sd, where hypocenters are deeper than in the other regions, the rupture strength is decreased by the presence of deep fluids, which may also account for the region being relatively susceptible to the influence of tidal forces. The fact that the *b*-value of the G-R law is

significantly large in region Sd is also consistent with the region being under high pore fluid pressure.

## Abbreviations

CFF	Coulomb failure function
CMT	Centroid moment tensor
G-R	Gutenberg–Richter
JMA	Japan Meteorological Agency
<i>M</i>	Magnitude
$M_{th}$	Threshold magnitude
$M_w$	Moment magnitude
NIED	National Research Institute for Earth Science and Disaster Resilience

## Acknowledgements

The program REASA (Aketagawa et al. 2007) was used to perform the Kolmogorov–Smirnov test and estimate the *b*-values of the G-R law. Figures were drawn with GMT (Wessel et al. 2013). The earthquake catalog is produced by the JMA in cooperation with MEXT. This manuscript was greatly improved by careful reviews of two anonymous reviewers.

## Author contributions

HF analyzed the data, wrote most of the manuscript, and made the figures and tables. TK proposed the *b*-value analysis, offered suggestions about the organization of the manuscript, and helped with the preparation of the manuscript. KA offered suggestions about the organization of the manuscript and helped with the preparation of the manuscript. MK offered suggestions about the organization of the manuscript and helped with the preparation of the manuscript. All authors read and approved the final manuscript.

## Funding

This research was conducted with support from the Japan Meteorological Agency.

## Availability of data and materials

The TidalStrain.2 program used to calculate theoretical tidal stresses is available for download from the Meteorological Research Institute repository (<https://mri-2.mri-jma.go.jp/owncloud/s/tjqx7HfK8bD3KQf>). The earthquake catalog used in this study is available at the Data Management Center of NIED (<https://www.hinet.bosai.go.jp/?LANG=en>) and JMA ([https://www.data.jma.go.jp/svd/eqev/data/bulletin/index\\_e.html](https://www.data.jma.go.jp/svd/eqev/data/bulletin/index_e.html)).

## Declarations

### Ethics approval and consent to participate

Not applicable.

### Consent for publication

Not applicable.

### Competing interests

The authors have no competing interests.

### Author details

<sup>1</sup>Meteorological Research Institute, Japan Meteorological Agency, 1-1 Nagamine, Tsukuba, Ibaraki 305-0052, Japan. <sup>2</sup>Matsushiro Seismological Observatory, Japan Meteorological Agency, 1-8-18 Hakoshimizu, Nagano, Nagano 380-0801, Japan.

Received: 10 December 2023 Accepted: 16 February 2024

Published: 28 February 2024

## References

- Aketagawa T, Ito H, Hirose F (2007) Development of REASA, an X Window program for retrieval of earthquake data and analysis of seismic activities (in Japanese). *Kenshin Zihou* (quart J Seismol) 70:51–66. <https://www.jma.go.jp/jma/kishou/books/kenshin/vol70p051.pdf>
- Aki K (1965) Maximum likelihood estimate of  $b$  in the formula  $\log N = a - bM$  and its confidence limits. *Bull Earthq Res Inst* 43:237–239. <https://doi.org/10.1508/0000033631>
- Amezawa Y, Hiramatsu Y, Miyakawa A, Imanishi K, Otsubo M (2023) Long-living earthquake swarm and intermittent seismicity in the northeastern tip of the Noto Peninsula, Japan. *Geophys Res Lett* 50:e2022GL102670. <https://doi.org/10.1029/2022GL102670>
- De Natale G, Zollo A (1986) Statistical analysis and clustering features of the Phlegraean fields earthquakes sequence (MAY 1983–May 1984). *Bull Seism Soc Am* 76(3):801–814. <https://doi.org/10.1785/BSSA0760030801>
- Dieterich J (1994) A constitutive law for rate of earthquake production and its application to earthquake clustering. *J Geophys Res* 99(B2):2601–2618. <https://doi.org/10.1029/93JB02581>
- Gutenberg B, Richter CF (1944) Frequency of earthquakes in California. *Bull Seism Soc Am* 34(4):185–188. <https://doi.org/10.1785/BSSA0340040185>
- Han J, Vidale JE, Houston H, Schmidt DA, Creager KC (2018) Deep long-period earthquakes beneath Mt. St. Helens: their relationship to tidal stress, episodic tremor and slip, and regular earthquakes. *Geophys Res Lett* 45:2241–2247. <https://doi.org/10.1002/2018GL077063>
- Heaton TH (1975) Tidal triggering of earthquakes. *Geophys J Int* 43(2):307–326. <https://doi.org/10.1111/j.1365-246X.1975.tb00637.x>
- Hirose F, Maeda K, Kamigaichi O (2019) Tidal forcing of interplate earthquakes along the Tonga-Kermadec Trench. *J Geophys Res* 124:10498–10521. <https://doi.org/10.1029/2019JB018088>
- Houston H (2015) Low friction and fault weakening revealed by rising sensitivity of tremor to tidal stress. *Nature Geo* 8:409–415. <https://doi.org/10.1038/ngeo2419>
- Iwata T, Nakanishi I (1998) Correlation between Earth tide and occurrences of earthquakes in Matsushiro area, Nagano, Japan (in Japanese with English abstract). *Zisin (J Seismol Soc Jpn 2nd Ser)* 51:51–59. [https://doi.org/10.4294/zisin1948.51.1\\_51](https://doi.org/10.4294/zisin1948.51.1_51)
- Japan Meteorological Agency (2023a) Seismic activity in and around the Kanto and Chubu districts (May–October 2022) (in Japanese). Report of the Coordinating Committee for Earthquake Prediction 109:116–176. [https://cais.gsi.go.jp/YOCHIREN/report/kaihou109/04\\_01.pdf](https://cais.gsi.go.jp/YOCHIREN/report/kaihou109/04_01.pdf).
- Japan Meteorological Agency (2023b) The seismological bulletin of Japan. [https://www.data.jma.go.jp/svd/eqev/data/bulletin/index\\_ehtml](https://www.data.jma.go.jp/svd/eqev/data/bulletin/index_ehtml). Accessed 3 Oct 2023
- Miguelanz L, González PJ, Tiampo KF, Fernández J (2021) Tidal influence on seismic activity during the 2011–2013 El Hierro volcanic unrest. *Tectonics* 40:e2020TC006201. <https://doi.org/10.1029/2020TC006201>
- Miguelanz L, Fernández J, Prieto JF, Tiampo KF (2023) Tidal modulation of the seismic activity related to the 2021 La Palma volcanic eruption. *Sci Rep* 13:6485. <https://doi.org/10.1038/s41598-023-33691-1>
- Nagata K, Tamaribuchi K, Hirose F, Noda A (2022) Statistical study on the regional characteristics of seismic activity in and around Japan: frequency-magnitude distribution and tidal correlation. *Earth Planets Space* 74:179. <https://doi.org/10.1186/s40623-022-01722-2>
- Nakajima J (2022) Crustal structure beneath earthquake swarm in the Noto peninsula. *Japan Earth Planets Space* 74:160. <https://doi.org/10.1186/s40623-022-01719-x>
- Nakata R, Suda N, Tsuruoka H (2008) Non-volcanic tremor resulting from the combined effect of Earth tides and slow slip events. *Nature Geosci* 1:676–678. <https://doi.org/10.1038/ngeo288>
- Nishimura T, Hiramatsu Y, Ohta Y (2023) Episodic transient deformation revealed by the analysis of multiple GNSS networks in the Noto Peninsula, central Japan. *Sci Rep* 13:8381. <https://doi.org/10.1038/s41598-023-35459-z>
- Ohtake M (1974) Seismic activity induced by water injection at Matsushiro, Japan. *J Phys Earth* 22:163–176. <https://doi.org/10.4294/jpe1952.22.163>
- Omureliava AM, Hasegawa A, Matsuzawa T, Nakajima J, Okada T (2012) Lateral variation of the cutoff depth of shallow earthquakes beneath the Japan Islands and its implications for seismogenesis. *Tectonophys* 518–521:93–105. <https://doi.org/10.1016/j.tecto.2011.11.013>
- Schuster A (1897) On lunar and solar periodicities of earthquakes. *Proc R Soc London* 61:455–465. <https://doi.org/10.1098/rspa.1897.0060>
- Spada M, Tornmann T, Wiemer S, Enescu B (2013) Generic dependence of the frequency-size distribution of earthquakes on depth and its relation to the strength profile of the crust. *Geophys Res Lett* 40(4):709–714. <https://doi.org/10.1029/2012GL054198>
- Tanaka S, Ohtake M, Sato H (2002) Evidence for tidal triggering of earthquakes as revealed from statistical analysis of global data. *J Geophys Res* 107:B102211. <https://doi.org/10.1029/2001JB001577>
- Terakawa T, Matsusura M (2022) Tectonic stress fields inferred from long-term CMT data ranging over different periods. *Geophys J Int* 233(1):162–181. <https://doi.org/10.1093/gji/gjac449>
- Utsu T (1965) A method for determining the value of  $b$  in a formula  $\log N = a - bM$  showing the magnitude-frequency relation for earthquakes (in Japanese with English abstract). *Geophys Bull Hokkaido Univ* 13:99–103. <https://doi.org/10.14943/gbh.13.99>
- Wessel P, Smith WHF, Scharroo R, Luis J, Wobbe F (2013) Generic mapping tools: improved version released. *Eos Trans AGU* 94:409–410. <https://doi.org/10.1029/2013EO450001>
- Wiemer S, Katsumata K (1999) Spatial variability of seismicity parameters in aftershock zones. *J Geophys Res* 104(B6):13135–13151. <https://doi.org/10.1029/1999JB900032>
- Woessner J, Wiemer S (2005) Assessing the quality of earthquake catalogues: estimating the magnitude of completeness and its uncertainty. *Bull Seism Soc Am* 95(2):684–698. <https://doi.org/10.1785/0120040007>
- Wyss M, Shimazaki K, Wiemer S (1997) Mapping active magma chambers by  $b$  values beneath the off-Ito volcano, Japan. *Japan J Geophys Res* 102(B9):20413–20422. <https://doi.org/10.1029/97JB01074>
- Wyss M, Hasegawa A, Nakajima J (2001) Source and path of magma for volcanoes in the subduction zone of northeastern Japan. *Geophys Res Lett* 28(9):1819–1822. <https://doi.org/10.1029/2000GL012558>
- Yabe S, Tanaka Y, Houston H, Ide S (2015) Tidal sensitivity of tectonic tremors in Nankai and Cascadia subduction zones. *J Geophys Res* 120:7587–7605. <https://doi.org/10.1002/2015JB012250>
- Yoshida N, Okusawa T, Tsukahara H (2002) Origin of deep Matsushiro earthquake swarm fluid inferred from isotope ratios. (in Japanese with English abstract). *Zisin (J Seismol Soc Jpn 2nd Ser)* 55:207–216. [https://doi.org/10.4294/zisin1948.55.2\\_207](https://doi.org/10.4294/zisin1948.55.2_207)
- Yoshioka R, Okuda S, Kitano Y (1970) Calcium chloride type water discharged from the Matsushiro area in connection with swarm earthquakes. *Geochem J* 4(2):61–74. <https://doi.org/10.2343/geochemj.4.61>

## Publisher's Note

Springer Nature remains neutral with regard to jurisdictional claims in published maps and institutional affiliations.